Atmospheric Research 270 (2022) 106059

Contents lists available at ScienceDirect

Atmospheric Research

journal homepage: www.elsevier.com/locate/atmosres

Integrated water vapor over the Arctic: Comparison between radiosondes and sun photometer observations

Juan Carlos Antuña-Marrero [a,*], Roberto Román [a], Victoria E. Cachorro [a], David Mateos [a], Carlos Toledano [a], Abel Calle [a], Juan Carlos Antuña-Sánchez [a], Javier Vaquero-Martínez [b,c], Manuel Antón [b,c], Ángel M. de Frutos Baraja [a]

[a] Group of Atmospheric Optics (GOA-UVa), Universidad de Valladolid, 47011 Valladolid, Spain
[b] Department of Physics, Universidad de Extremadura, 06006 Badajoz, Spain
[c] Instituto Universitario de Investigación del Agua, Cambio Climático y Sostenibilidad (IACYS), Universidad de Extremadura, 06006 Badajoz, Spain

ARTICLE INFO

Keywords:
Integrated water vapor
Arctic
Sun photometer
Radiosonde
AERONET

ABSTRACT

The amplification of global warming because of the feedbacks associated with the increase in atmospheric moisture and the decrease in sea ice and snow cover in the Arctic is currently the focus of scientists, policy makers and society. The amplification of global warming is the response to increases in precipitation originally caused by climate change. Arctic predominant increases in specific humidity and precipitation have been documented by observations. In comparison, evapotranspiration in the Arctic is poorly known, in part, because the spatial and temporal sparsity of accurate in situ and remote sensing observations. Although more than 20 observations sites in the Arctic are available, where AERONET sun photometer integrated water vapor (IWV) measurements have been conducted, that information have been barely used. Here, we present a comparison of IWV observations from radiosondes and AERONET sun photometers at ten sites located across the Arctic with the goal to document the feasibility of that set of observations to contribute to the ongoing and future research on polar regions. Sun photometer IWV observations are averaged for three-time windows; 30 min, 6 and 24 h. The predominant dry bias of AERONET IWV observations with respect to radiosondes, identified at tropical and midlatitudes, is also present in the Arctic. The statistics of the comparison show robust results at eight of the ten sites, with precision and accuracy magnitudes below 8 and 2% respectively. The possible causes of the less robust results at the other two sites are discussed. In addition, the impact of selecting other temporal coincidence windows in the average sun photometer IWV used in the comparison were tested. Auto-correlation in diurnal sun photometer IWV could produce appreciable bias in the statistics used for the comparison. We suggest using only one pair of values per day, consisting in the daily mean IWV sun photometer and the IWV radiosonde observation value. This feature should be valid also for comparison of IWV from sun photometer and other instruments. Maximum 10% error level of IWV from sun photometer observations, when compared with radiosondes, have been found for the Arctic. It is in the same order of magnitude than at tropical and middle latitudes locations. It has been demonstrated the feasibility of AERONET IWV observations in the Arctic for research on this variable. AERONET standard instruments and its centralized-standard processing algorithm allow its IWV observations to be considered a relative standard dataset for the re-calibration of other instrumental IWV observations assuming radiosondes as the absolute standard dataset.

1. Introduction

Water vapor is the main natural greenhouse gas in the Earth's atmosphere. It absorbs longwave radiation and radiates part of it back to the Earth's surface, contributing to climate warming (Forster et al., 2007). Climate warming has been predicted to introduce changes in the hydrological cycle globally (Collins et al., 2013) and particularly in the Arctic (Bintanja and Selten, 2014). The analysis of key observational indicators in the Arctic, most of them monitored since 1971, demonstrated fundamental changes. Among them, the intensification of the

* Corresponding author.
E-mail address: antuna@goa.uva.es (J.C. Antuña-Marrero).

https://doi.org/10.1016/j.atmosres.2022.106059
Received 21 September 2021; Received in revised form 4 January 2022; Accepted 27 January 2022
Available online 2 February 2022

hydrological cycle, associated to observed increasing temperatures, is evident from the increase in humidity, precipitation, river discharge, glacier equilibrium line altitude and land ice wastage (Box et al., 2019).

Recent research reviewed the atmospheric role in the Arctic water cycle, finding from the observational evidence that in general for recent decades the specific humidity and precipitation have increased (Vihma et al., 2016). However, the changes in evapotranspiration are poorly known, being among the main reasons the sparsity (in space and time) of accurate in situ and remote sensing observations. Large errors and uncertainties in the Arctic in atmospheric reanalysis are also cited and attributed to the lack of reliable observations and to the inhomogeneity of the data during the entire analysis period using state-of-the-art assimilation methods (Vihma et al., 2016).

A broad range of ground-based techniques are being currently used for water vapor observations: sun photometry (e.g. Alexandrov et al., 2009), radiosondes (e.g. Durre et al., 2006, 2009), Global Navigation Satellite System (GNSS) (e.g. Elgered et al., 1997; Vaquero-Martinez and Anton, 2021), Fourier transform spectrometers (Leblanc et al., 2011; Vogelmann et al., 2015), Microwave Radiometers (MWR) (e. g., Steinke et al., 2015) and Raman lidar systems (Whiteman et al., 2012; Vogelmann et al., 2015). Additionally, several satellite instruments provide accurate water vapor observations (e.g, Román et al., 2015; Vaquero-Martínez et al., 2018), with high spatial resolution worldwide including the Arctic region (Vaquero-Martínez et al., 2020). Operational radiosondes observations of the water vapor vertical profiles are the source of one of the main integrated water vapor (IWV) databases, the Integrated Global Radiosonde Archive −2; (IGRA-2) covering from the first half of the XX century to the present (Durre et al., 2006). Radiosonde IWV observations (IWV_{sonde}) commonly are assumed as the reference in comparison with other instruments (e. g. Pérez-Ramírez et al., 2014; Antón et al., 2015; Vaquero-Martínez et al., 2019).

According to the Global Energy and Water Exchanges (GEWEX) water vapor assessment (G-VAP) report, a consistent analysis of the quality of all mature and freely available long-term water vapor data records has not been carried out to date (Schröder et al., 2017). Integrated water vapor observations made from sun photometers in the Arctic are one of those datasets which has not been the subject of consistent analysis. The public archives of the NASA Aerosol Robotic Network (AERONET) contain observations from 24 sites north of 66.5°N with variable time covertures dating back, in some few sites, to 1997 (AERONET, 2021).

Sun photometers are easy to deploy and have a low cost compared with most of the other techniques described above. Solar direct irradiance measurements recorded by sun photometers in spectral channels, within water vapor absorption bands, can be used to retrieve the water vapor transmittance (Schmid et al., 2001). In the particular case of AERONET, they use the same state-of-the-art instruments, calibration procedures and algorithms for observations quality control and processing guarantying homogeneity and high quality in the total water vapor retrievals. The AERONET Version 3 algorithm retrieves the water vapor transmittance for the 935 nm channel using the absorption constants unique to the 935 nm filter, and then derives the total column water vapor abundance (u) and converts u to total column water vapor content or precipitable water vapor in centimeters (Giles et al., 2019). Although IWV_{SP} (Integrated Water Vapor derived from Sun Photometers) from AERONET shows consistent biases with respect to the rest of the ground-based and satellite instruments, they provide a unique homogeneous dataset, because of its standard instruments and its centralized-standard processing algorithm. These homogeneity features make IWV_{SP} observations from AERONET an ideal relative standard to extend the use of IWV observations by-ground based techniques in Arctic areas, thus increasing spatial coverage. The use of sun photometry to this end, instead the reference radiosonde, can be addressed if the uncertainty or possible bias are well known.

IWV observations from sun photometers at individual sites in the Arctic have already been used for comparisons with multiple instruments at global scale studies. Examples are the comparisons with IWV observations from MODIS satellite instruments (Bright et al., 2018; Wang and Liu, 2020), with GPS (Vaquero-Martinez and Anton, 2021) and with Fourier transform spectrometers (Weaver et al., 2017). In the Arctic, very few comparisons of the IWV observations from sun photometers with IWV observations from radiosondes, considered as the reference standard, have been reported. They were conducted at Barrow, Alaska (Pérez-Ramírez et al., 2014), at PEARL and 0PAL, Canada (Weaver et al., 2017), and Hornsund, Norway (Kruczyk and Liwosz, 2015). Several Arctic sun photometer series of IWV observations have been used in comparisons for broader regions of the world, but as part of dataset composites, with no available individual Arctic sites comparison statistics (e. g. Van Malderen et al., 2014; Gong et al., 2020).

In this framework, the main objective of this work is to compare radiosonde and sun photometer IWV observations in the Arctic to estimate the accuracy and precision of IWV_{SP} AERONET product in this important region. This paper is structured as follows: Section 2 describes the datasets, the coincidence criteria selected, and the processing and statistics chosen. Section 3 shows and discusses the main results, while Section 4 exposes and summarizes the conclusions.

2. Places, data, and method

2.1. Study area

Fig. 1 shows the geographical distribution of the 10 Arctic AERONET sites selected in this work. They extent across the Arctic from Barrow (Alaska; 156.66°W) to Tiksi (Russia; 128.92°E), and from Sodankyla (Norway; 67.37°N) to PEARL (Canada; 80.05°N). They were selected according to the following criteria: 1) location northernmost than 66.5°N (within Arctic circle) and 2) availability of radiosonde profiles at the site or within a radius below 100 km. Table 1 provides information about the geographical location and the main features of the IWV from sun photometer (IWV_{SP}) records for each site: latitude, longitude, altitude, total number of individual observations, total number days with observations, period of years covered by the observations and amount of years with observation in that period. Hornsund station does not satisfy the mentioned second criteria, because it is located at 230 km from the nearest sounding site: Ny-Ålesund-AWI; however, considering the

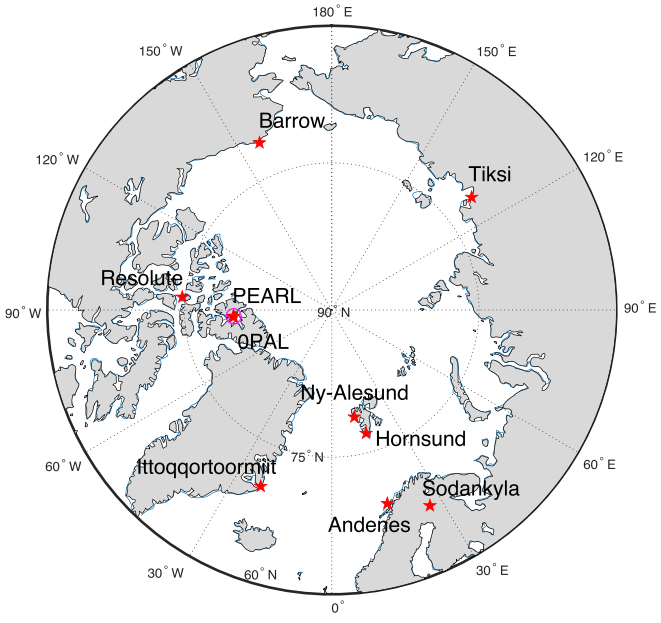

Fig. 1. Map of the Arctic showing the geographical locations of the sites used in the present study.

Table 1
The left section under AERONET shows for the sites where the sun photometers are located, its geographical locations, altitude (m), number of observations and days, period of years they cover and the total of years of data (in parenthesis). The right section under IGRA-2 show the sounding sites located in the vicinity of the sun photometer, the distance between both instrument as well as the altitude of the sounding and the altitude difference (in m) between the sounding site and the sun photometer (in parenthesis).

AERONET							IGRA-2		
Site	Lat (°N)	Long (°E)	Alt(m)	Observ.	Days	Period (Years)	Site	D(km)	Alt. (m)
Barrow	71.31	−156.66	8	30,547	1262	1997–2020(23)	Barrow	5.0	12(−4)
Resolute	74.71	−94.97	35	73,529	866	2004–2019(14)	Resolute	0.1	46(−11)
PEARL	80.05	−86.42	615	137,779	1104	2007–2019(12)	Eureka UA	12.2	10(605)
0PAL	79.99	−85.94	5	92,395	967	2007–2019(11)	Eureka UA	0.8	10(−5)
Ittoqqort.	70.48	−21.95	68	25,989	885	2010–2019(9)	Ittoqqort.	0.0	70(−2)
Ny Ålesund	78.92	11.92	7	4354	180	2017–2019(3)	Ny Ålesund	0.0	16(−9)
Hornsund	77.00	15.54	12	15,824	827	2004–2017(14)	Ny Ålesund	230.0	16(−4)
Andenes	69.28	16.01	379	37,463	1153	2002–2020(15)	Andoya	6.4	10(369)
Sodankyla	67.37	26.63	184	17,273	885	2007–2019(8)	Sodankyla	0.0	179(5)
Tiksi	71.59	128.92	17	4634	335	2010–2015 (6)	Tiksi	0.4	6 (11)

Integrated water vapor over the Arctic: Comparison between radiosondes and sun photometer observations.

reasonable results reported by Kruczyk and Liwosz (2015) comparing IWV_{SP} from Hornsund and IWV_{sonde} from Ny-Ålesund-AWI, we decided to include it.

2.2. Data and instrumentation

Sun photometry measurements of IWV are conducted at different water vapor wavelength-dependent absorption bands. The Cimel-318 sun photometer, AERONET standard instrument, uses the 935 nm wavelength as mentioned above. IWV_{SP} observations used in this study are from AERONET version 3, level 2.0 (Giles et al., 2019). The IWV_{sonde} dataset consists of eight radiosounding sites complying the second condition imposed in the selection of the IWV_{SP} dataset from the AERONET sites. Seven of the sites present radiosonde profiles in the site area. For the other 3 sites we used nearby soundings. For PEARL and 0PAL we used the IWV_{sonde} from Eureka at ~12 and 1 km of distance, respectively. The largest distance between sounding and photometer sites is the case of Hornsund, because the soundings are carried out in Ny-Ålesund about 230 km apart.

The IWV_{sonde} data used have been obtained from IGRA-2. The general information about the development, attributes and available information from IGRA dataset is provided in Durre et al. (2006). We used its updated version, IGRA-2, with an improved quality control in general (Durre et al., 2008; Durre et al., 2018). In particular, the quality controls of the relative humidity and dew point values introduced in the update from IGRA to IGRA-2 are exposed in detail in Durre et al. (2018). Once the quality control process is concluded, a large group of derived atmospheric variables is calculated, which are stored in a file for this purpose. The IWV is one of these variables and is calculated as stated by Durre et al. (2009). These data are stored in a NOAA-NCEP repository (Durre et al., 2016).

The altitude difference between the sun photometer located at PEARL (615 m asl) and the radiosonde facility at Eureka (10 m asl) is 605 m; this difference is 369 m between Andenes (379 m asl) and Andoya (10 m asl). Hence, the IWV_{Sonde} values were corrected to match the altitude of the sun photometer site. The procedure replicated the one current in place for IGRA-2 database (Durre et al., 2009). However, the vertical integration to calculate the IWV_{sonde} uses as its lower pressure level at each sounding the one corresponding to the altitude of the sun photometer site.

2.3. Spatiotemporal coincidence criteria

Radiosonde observations at 12:00 and 00:00 Universal Time Coordinated (UTC) are available at all sites. An important issue of the available Arctic sites compiled for this research is their distribution between two time zones associated to two geographical regions, Greenland and European Arctic (GEA), where the 12:00 UTC sounding coincide with the 12:00 Local Time (LT) at meridian 0°; while for eastern Russia, Alaska and Canadian Arctic (RACA), the 12:00 UTC sounding coincide with the 00:00 LT at meridian 180° E or W. This fact is important because the sun photometer observations are carried out when sunlight is available, making its observations dependent on the diurnal cycle. That can be seen in Fig. 2, that shows the hourly distribution of the IWV_{SP} for the 10 sites. For the RACA sites the number of observations around 12 UTC is minimum, while for the GEA it is maximum. Soundings at 00:00 UTC are, therefore, selected in the comparison for the RACA sites and those at 12:00 UTC are selected for GEA sites.

Radiosondes take approximately 30 min to make a complete atmospheric profile for the purposes of calculating IWV_{sonde}. Then, for a more accurate comparison, IWV_{SP} values from sun photometer observations have been averaged for the 30 min time window of the radiosonde measurements as in Pérez-Ramírez et al. (2014). In addition, two more time windows are used in this work around the radiosonde measurements: 6 h window (averaging from 09:00 to 15:00 LT) and daily window (averaging all available data, from 00:00 to 24:00, in the day of radiosonde). These averaged IWV_{SP} measurements are named as $\overline{IWV}_{SP}$.

2.4. Statistics

The chosen statistics for the comparison between IWV from radiosondes and photometers are: 1) the Mean Bias Error (MBE), which defines the mean of the differences between IWV_{sonde} and $\overline{IWV}_{SP}$ (ΔIWV), quantifying the accuracy on $\overline{IWV}_{SP}$; and 2) the standard deviation of the differences between IWV_{sonde} and $\overline{IWV}_{SP}$ (STD), which represents the precision of $\overline{IWV}_{SP}$. Both statistics are defined in Eqs. (1) and (2), respectively:

$$MBE = \frac{1}{N}\sum_{j=1}^{N}\left[\Delta IWV_j\right] \quad (1)$$

$$STD = \frac{1}{N}\sqrt{\sum_{j=1}^{N}\left[\Delta IWV_j - \overline{\Delta IWV}\right]^2} \quad (2)$$

where N is the number of the pairs of coincident IWV_{sonde} and $\overline{IWV}_{SP}$values, ΔIWV_j is the $IWV_{sonde,j} - \overline{IWV}_{SP,j}$ difference of the j-element, and $\overline{\Delta IWV}$ is the mean value of the N values of ΔIWV_j. The relative magnitudes (in %) of STD (rSTD) and MBE (rMBE) are determined dividing each of them by the mean value of the N observations of IWV_{sonde} ($\overline{IWV}_{sonde}$). In addition, the Pearson linear correlation coefficient (R) and the slope of the linear regression fit between IWV_{sonde} and $\overline{IWV}_{SP}$ have been calculated. The relative error estimates (RE), in %, for each pair of IWV_{sonde} and $\overline{IWV}_{SP}$ values are calculated using the

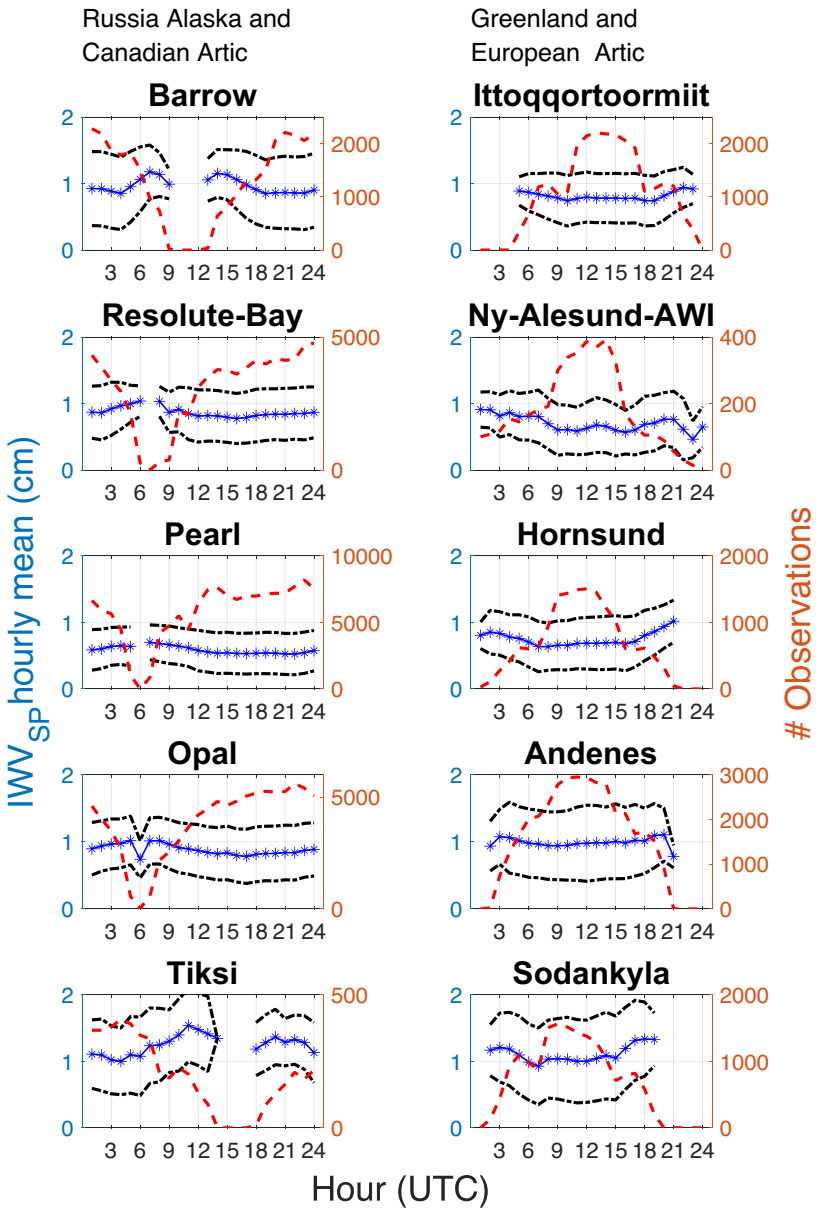

Fig. 2. Diurnal variability of the IWV_{SP} for all the sites. IWV_{SP} hourly mean values (blue stars) and its σ (discontinuous black lines). The hourly number of observations is shown (red discontinuous line). (For interpretation of the references to colour in this figure legend, the reader is referred to the web version of this article.)

following expression:

$$RE = \frac{IWV_{sonde} - \overline{IWV}_{SP}}{IWV_{sonde}} \text{ x } 100 \quad (3)$$

3. Results

3.1. Hourly IWV_{sp} and diurnal cycle

Before the comparison between sun photometer and radiosonde IWV data, an analysis about the IWV_{SP} data is carried out to study the available data. In this sense, Fig. 2 shows the hourly means of IWV_{SP} using all the available observations for each site. The hourly number of observations and the diurnal variability of the IWV_{SP} for each the site ($\overline{IWV}_{SP} \pm \sigma_{IWV_{SP}}$,where $\sigma_{IWV_{SP}}$is the $\overline{IWV}_{SP}$standard deviation, are also depicted. The latitudinal sites distribution, causing the midnight sun in summer, produces a unique polar pattern of almost 20 or more hours of available sun photometer observations. Along the year available observations are constrained to parts of the spring and autumn and the whole summer. At RACA sites the gaps in observations are located around the 12:00 UTC, with the higher observations amounts around 00:00 UTC. At the GEA sites, the pattern is the opposite, higher observation amounts around 12:00 UTC and gaps around 00:00 UTC.

Table S1 in the Supplement shows the statistics at each site derived from the hourly means IWV_{SP}, reported on Fig. 2. The sites showing more variability are Tiksi, Sodankyla, Barrow and Ny-Ålesund, with the first three of them showing the higher multi hour IWV_{SP} means with values of 1.25 ± 0.15 cm, 1.11 ± 0.13 cm and 0.97 ± 0.11 cm. In the case of Ny-Ålesund, the IWV_{SP} mean is 0.70 ± 0.12 cm, the second lowest value, and the number of observations is the lowest: 4354 (180 days). The other sites on Table S1with lower variability have also IWV_{SP} mean lower than 1.0 cm. The IWV_{SP} means for RACA and GEA show values of 0.91 ± 0.07 cm and 0.85 ± 0.07 cm respectively, being the IWV_{SP} mean for all the sites together 0.88 ± 0.04 cm.

It should be considered the fact that the amount of available hourly

IWV_{SP} observations, denoted by the discontinuous red line in Fig. 2, depends on the Arctic geographical location. Maximum and minimum hourly IWV_{SP} observations occur around local noon and night respectively at each site. Absolute maximums (like at Resolute Bay) and minimums (like at 0Pal and Ny-Ålesund) in Fig. 2 are more plausibly associated to biased averages, produced by the decay in 2 or more orders of magnitude in the number of available observations.

3.2. IWV from sun photometer vs. radiosonde

The sun photometer and radiosonde comparison was conducted considering the mean values in three temporal windows explained above. The resulting sets of available mean IWV_{SP} values in the three time windows were classified in two groups. The first group, named "unconstrained", consisted in all the available mean IWV_{SP} values in the three time windows, and the statistics study is shown in Table 2. The second group, named "constrained" only included the days having IWV_{SP} observations at the three temporal windows (30 min, 6 h and 24 h), shown on Table S2 in the Supplement.

The left section on Table 2 shows the statistics for the 30 min temporal window. The STD (rSTD) values ranges from 0.03 cm (4.1%) at Ny-Ålesund to 0.18 cm (25%). at Hornsund, with 80% of the sites having STD (rSTD) values below or equal to 0.10 cm (10%) Hornsund and Tiksi show higher values.

The MBE (rMBE) is between 0.04 cm (4.4%) at Resolute and − 0.19 cm (−13.9%) at Tiksi, with positive values at Resolute and 0PAL pointing out higher values of IWV_{SP} than IWV_{sonde} at both sites. The other sites show absolute values of MBE (rMBE) below −0.05 cm (−5.0%) except at Tiksi.

The slopes of the linear regression fits range between 1.01 at Resolute to 0.83 at Hornsund, with Tiksi and Hornsund below 0.90 and the rest of the sites above this value. The intercepts of the linear fits are close to 0 (<0.04 cm) with the exception of Hornsund. As expected from these results, correlation coefficient R shows the lower values at Hornsund (0.92) and Tiksi (0.96) while at the rest of the sites it is equal or higher than 0.99.

Regarding the other temporal windows, the magnitudes of STD and MBE increase at all the sites respect to 30-min averages. Also, at the same time, the magnitudes of the R and slope decrease in general too. It is worth remembering that the statistics for both longer temporal windows have been calculated using all the available daily IWV_{SP}, what assumes that there are observations in one or two of the other windows or in other parts of the day. When we imposed the constrain to use only days with IWV_{SP} observations in all 3 temporal windows, the statistics at all the sites showed little variation at the 3 temporal windows, as can be seen in Table S2. This fact is the result of the high level of autocorrelation between the IWV_{SP} hourly observations already found by Steinke et al., (2015) and imposes notable limitation in the selection of temporal coincidence criteria for comparisons and for the production of climate data records.

In general, the statistics for the individual Arctic sites show a good agreement between the IWV_{sonde} and IWV_{SP}, except for Tiksi and Hornsund, with errors in the range between 5 and 10% in line with the results reported by Alexandrov et al. (2009), Pérez-Ramírez et al. (2014) and Berezin et al. (2017). The analysis of the statistics also confirms sun photometer observations underestimating radiosonde observations of IWV, in line with previous studies in Arctic region (e.g. Schneider et al., 2010; Pérez-Ramírez et al., 2012; Weaver et al., 2017).

Table 2 also lists the statistics results for the two time zone regions: Russia, Alaska and Canadian Arctic (RACA) and Greenland and European Arctic (GEA), as well as for all the sites together. At the 30 min time window there are almost unnoticeable differences between both regions, no matter that there are 20% more observations at RACA than at GEA. The results of the statistics for all the sites together show almost no difference at all between the results at RACA and GEA, as expected, because of the existence of almost no difference between both time zone

Table 2

Statistics of the comparison of $\overline{IWV_{SP}}$ *vs* IWV_{sonde} for each site/region for the three-time windows used to calculate $\overline{IWV_{SP}}$ for all the available observations. For STD and MBE the first value is the magnitude of the statistic (cm) and the second in parenthesis is the relative value (%), using the $\overline{IWV_{sonde}}$ for the normalization. In the case of the linear fit, $\overline{IWV_{SP}}$ *vs* IWV_{sonde}, the first value is the slope and the one in parenthesis the intercept.

UNCONSTRAINED TEMPORAL WINDOWS															
Site/Region	30 min					09–15 LT					00–24 LT				
	STD/ cm (%	MBE/cm (%)	Linear Fit	R	N	STD/ cm (%)	MBE/cm (%)	Linear Fit	R	N	STD/ cm (%)	MBE/cm (%)	Linear Fit	R	N
Barrow	0.10 (10.1)	−0.04 (−3.8)	0.93 (0.03)	0.99	409	0.37 (34.2)	−0.07 (−6.7)	0.73 (0.22)	0.80	813	0.35 (31.5)	−0.09 (−8.1)	0.72 (0.22)	0.81	1069
Resolute	0.05 (5.8)	0.04 (4.4)	1.01 (0.03)	0.99	315	0.25 (27.5)	−0.03 (−2.8)	0.76 (0.19)	0.81	516	0.26 (28.4)	−0.04 (−4.8)	0.73 (0.20)	0.81	760
PEARL	0.04 (7.0)	−0.01 (−1.3)	0.96 (0.02)	0.99	516	0.18 (29.2)	−0.03 (−4.4)	0.78 (0.10)	0.86	750	0.18 (28.4)	−0.05 (−7.2)	0.75 (0.11)	0.87	960
0PAL	0.05 (6.1)	0.01 (0.8)	0.96 (0.04)	0.99	344	0.20 (22.2)	−0.03 (−2.7)	0.81 (0.15)	0.88	592	0.20 (22.4)	−0.04 (−5.0)	0.79 (0.14)	0.89	828
Tiksi	0.17 (12.0)	−0.19 (−13.9)	0.86 (0.00)	0.96	74	0.46 (34.2)	−0.22 (−16.6)	0.58 (0.34)	0.72	182	0.49 (36.3)	−0.18 (−12.9)	0.59 (0.38)	0.68	280
RACA	0.09 (10.4)	−0.01 (−1.4)	0.93 (0.04)	0.98	1658	0.29 (31.2)	−0.05 (−5.7)	0.75 (0.17)	0.84	2853	0.28 (30.9)	−0.07 (−7.2)	0.74 (0.17)	0.84	3897
Ittoqqortoo.	0.05 (6.1)	−0.01 (−1.0)	0.96 (0.03)	0.99	474	0.08 (9.6)	−0.01 (−1.1)	0.93 (0.05)	0.98	733	0.11 (12.8)	−0.03 (−3.3)	0.88 (0.08)	0.97	865
Ny_Ålesund	0.03 (4.1)	−0.01 (−0.8)	0.96 (0.02)	1.00	56	0.06 (8.6)	−0.02 (−2.3)	0.93 (0.03)	0.99	130	0.14 (17.5)	−0.04 (−5.7)	0.86 (0.07)	0.95	168
Hornsund	0.18 (25.0)	−0.03 (−3.9)	0.83 (0.09)	0.92	224	0.18 (24.1)	−0.01 (−1.5)	0.85 (0.10)	0.91	545	0.18 (23.4)	−0.03 (−3.6)	0.82 (0.12)	0.91	730
Andenes	0.06 (5.7)	−0.02 (−2.3)	0.95 (0.02)	1.00	231	0.08 (8.3)	−0.03 (−3.5)	0.93 (0.03)	0.99	395	0.15 (15.2)	−0.08 (−7.5)	0.86 (0.07)	0.97	486
Sodankyla	0.07 (6.7)	−0.04 (−3.9)	0.94 (0.02)	0.99	329	0.12 (10.3)	−0.07 (−6.3)	0.91 (0.03)	0.98	661	0.20 (16.0)	−0.12 (−9.7)	0.84 (0.08)	0.96	858
GEA	0.09 (10.5)	−0.02 (−2.5)	0.93 (0.04)	0.99	1314	0.12 (13.3)	−0.03 (−3.4)	0.90 (0.06)	0.98	2464	0.17 (17.5)	−0.06 (−6.4)	0.84 (0.09)	0.96	3107
ALL sites	0.09 (10.4)	−0.02 (−1.9)	0.93 (0.00)	0.99	2972	0.23 (25.8)	−0.05 (−6.0)	0.79 (0.10)	0.89	5317	0.24 (25.6)	−0.06 (−6.8)	0.79 (0.10)	0.90	7004

regions. The Figure S1 (in the Supplement) shows the scattering plots and the linear fits for each one of the ten individual stations and for both GEA and RACA regions illustrating the results discussed in this section.

Table 3 we show the statistics and the linear regression results for the three regions both considering all the 10 sites (ALL sites(1)) and also excluding Tiksi and Hornsund (ALL sites(2)). We see a decrease in STD (rSTD) in the range of 0.09 to 0.07 cm (10 to 8%). For the MBE (rMBE) the improvement is from −0.02 to −0.01 cm (−2 to −1%), with little improvements in the slope and intercept of the linear regression fit and no improvement in R. It is notable that the rSTD for all the sites together, excluding Tiksi and Hornsund which have the highest error levels, is below 8%.

If only the data when the three temporal windows are considered (Table S2) the total number of pairs of IWV_{sonde} and $\overline{IWV_{sp}}$ for all the sites together decreases by 8% (2972 in Table 2 to 2739 in Table S2) for the 30-min window; however, all the statistics remain in the same order of magnitude and in general with very little changes in its values, showing the robustness of the results for this temporal window.

Fig. 3 shows the scattering plot of IWV_{sonde} vs. $\overline{IWV_{sp}}$ coincident in the 30 min constrained time windows for all the Arctic stations, except Hornsund and Tiksi. The linear fit shows a high value of the Pearson correlation coefficient (0.992). The low value of the intercept (0.032 cm) and the small dispersion around the fitted line completes the characterization of the good agreement between the observations from both instruments. The slope of the linear fit is 0.95, pointing out that IWV_{sonde} slightly underestimates IWV_{SP} values.

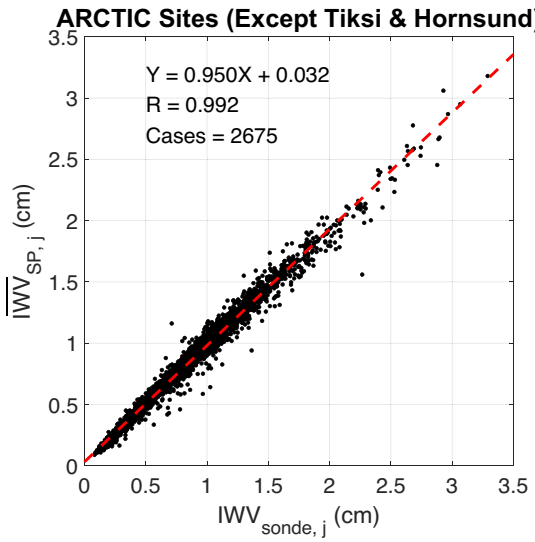

Fig. 3. Scattering plot of $\overline{IWV_{sp}}$ vs.IWV_{sonde}. for all the coincident pairs in the 30 min time windows (unconstrained) for all the Arctic stations, except Hornsund and Tiksi. The linear fit is also shown by the discontinuous red line together with the values for the slope, intercept and the Pearson linear correlation coefficient (R), reported on Table 3 as "ALL sites(2)". (For interpretation of the references to colour in this figure legend, the reader is referred to the web version of this article.)

3.3. Comparison with other studies

IWV_{SP} and IWV_{sonde} comparisons were carried out at Barrow (Pérez-Ramírez et al., 2014), Hornsund (Kruczyk and Liwosz, 2015), and 0PAL and PEARL (Weaver et al., 2017). Pérez-Ramírez et al. (2014) used for Barrow a total of 399 pairs of $\overline{IWV_{sp}}$ (30-min window) and IWV_{sonde} (4 daily radiosondes) data for the period 2002–2011. They obtained a STD value of 0.07 cm, which is similar to the obtained in our study: 0.10 cm (see Table 2). The MBE was −0.02 cm while in our study it is −0.04 cm.

Weaver et al. (2017) developed a validation of IWV_{SP} with IWV_{sonde} at PEARL (March 2007 to September 2015) and 0PAL (April 2007 to September 2013) with IWV_{sonde} measured from Eureka and using the IWV_{SP} nearest in time to the radiosonde within ±2 h. They recalculated the values of IWV_{sonde} for the PEARL site by an altitude correction (Weaver et al., 2017).

At PEARL, with 1038 coincident data pairs of IWV_{sonde} and IWV_{SP}, Weaver et al. (2017) reported STD, slope and R values equal to 0.06 cm, 0.90 and 0.99, respectively; while the results for the same statistics in the present work are slightly better: 0.04 cm, 0.96 and 0.99 (see Table 2). The absolute MBE of 0.039 cm reported by Weaver et al. (2017) matches the same order of magnitude than the MBE of −0.01 cm of Table 2. Weaver et al. (2017) used 692 coincident data pairs of IWV_{sonde} and IWV_{SP} for 0PAL; they reported STD, slope and R statistics about 0.067 cm, 0.93 and 0.99, respectively, while these values are in the present work also slightly better: 0.05 cm, 0.96 and 0.99. Regarding MBE at 0PAL, both obtained values (Weaver et al., 2017; and this work) are close to zero.

In the reported studies for Barrow (Pérez-Ramírez et al., 2014), PEARL and 0PAL (Weaver et al., 2017) they used all the available soundings without any constrain. The rates of the amount of coincident data pairs to the extension of the period of observation in their study for both stations are higher than the same rate in this study because we only selected the 12 LT sounding each day. It has been shown a reasonable agreement between the statistics calculated in this study and the reported validations at four of the sites.

Regarding Hornsund, Kruczyk and Liwosz (2015) compared 187 data pairs of IWV_{SP} and IWV_{sonde} for the period 2005–2010, reporting a STD value of 0.17 cm and a negative MBE of −0.008 cm. These values are similar to those shown in Table 2: 0.18 cm and − 0.03 cm, respectively. However, as it has been shown above, those results are the worst in the comparison with other sites. In the following section we discussed the possible causes.

It should be considered that previous studies using AERONET version 2.0 products only included IWPSP data up to an optical air mass of 5. The recent version 3.0 of AERONET products extended the observations up to an optical air mass of 7 (Giles et al., 2019). This optical air mass range increase produces an increment in the number of solar measurements occurring at higher solar zenith angles, what in terms of the diurnal cycle means the early morning and the early evening both aerosol optical depth and IWV_{SP} observations. That increase in the number of available IWV_{SP} daily observations in Version 3 with respect to Version 2, together with changes in quality control procedures and IWV_{SP} calculus improvements (Giles et al., 2019) increase notably the sources of potential differences between the statistic's derived in the present comparison and the three former comparisons cited above. Those reasons described above are the same why we did not attempt to conduct $\overline{IWV_{SP}}$ comparisons between the current set of observations and the ones reported before in the literature.

Table 3
Statistics and linear fit regression results for each region for all the available observations in the 30 min time window. The three top regions account for the 10 sites used above(1) in Table 2, while in the lower three Tiksi and Hornsund sites were excluded(2).

Site/Region	30 min				
	STD/cm (%)	MBE/cm (%)	Linear Fit	R	N
RACA(1)	0.09 (10.4)	−0.01 (−1.4)	0.93 (0.04)	0.98	1658
GEA(1)	0.09 (10.5)	−0.02 (−2.5)	0.93 (0.04)	0.99	1314
ALL sites(1)	0.09 (10.4)	−0.02 (−1.9)	0.93 (0.00)	0.99	2972
RACA(2)	0.07 (8.6)	−0.00 (−0.4)	0.96 (0.03)	0.98	1584
GEA(2)	0.06 (6.5)	−0.02 (−2.3)	0.95 (0.03)	0.99	1090
ALL sites(2)	0.07 (7.8)	−0.01 (−1.2)	0.95 (0.03)	0.99	2675

3.4. Hornsund and Tiksi

To our knowledge, this is the first multisite long-term comparison of IWV observations by radiosondes and sun photometers in the Arctic. It has been preceded by reports of few individual comparisons, discussed above, whose results match the results reported here. There are two sites which do not match the general pattern of precision and accuracy features: Hornsund and Tiksi. These two sites show higher errors both in precision and accuracy in the comparisons at almost all the time windows, both for constrained and not constrained cases.

Hornsund shows STD (rSTD) values of 0.18 cm (~25%) in Table 3 and Table S1 for the not constrained and constrained cases. Similarly for MBE (rMBE) its values are −0.03 cm and (~ −4%) in Table S1. The main reasons are the distance between the IWV_{SP} observations at Hornsund and the IWV_{sonde} observations at Ny-Ålesund (230 km) together with the different geographical conditions between both sites (see Fig. 1). Hornsund is located in the southern part of Spitsbergen, a narrow area of the island, surrounded major part of the year by unfrozen water. At Ny-Ålesund the open sea is only near at its west side that is covered by sea ice from January to June at this latitude. In addition, at this site there is much more land in its side than at Hornsund. All these conditions, together with the predominant eastward wind direction, are the causes of a more continental climate at Ny-Ålesund than at Hornsund. The relative humidity shows higher values at Hornsund than at Ny-Ålesund, according to reports from 1975 to 2000 (Przybylak and Araźny, 2006) and from 2005 to 2016 (Cisek et al., 2017), with higher values in the last period. Those higher values at Hornsund are in line with the results shown in Fig. 2 and the statistics results on Table 2 and Table S1. The fact is: we are sampling the IWV at distant sites at a spatial scale with a high variability of IWV associated to the main drivers of the Arctic atmospheric water cycle. Those drivers mainly the polar jet stream, storm tracks, and related phenomena operate at scales ranging from mesoscale to synoptic-scale (Bintanja and Selten, 2014).

Tiksi shows similar differences between sun photometer and radiosondes to Hornsund, being higher than the rest of the sites. It is shown in the magnitudes of the STD (rSTD) statistics, with values of 0.17 cm (~12.0%) and in MBE (rMBE) of −0.19 cm (~ −14%) for the not constrained and constrained 30 min time window (Table 3 and Table S1). Among the possible reasons for such behavior can be the low amount of IWV_{SP}-IWV_{sonde} data pairs (74) of. However, Ny-Ålesund presents less amount of data pairs (56) and it showed the lowest errors. Hence, it will be very unlikely that the low amount of data pairs could be the cause of the high discrepancy between photometer and radiosonde at Tiksi.

Another possibility is related to the higher errors attributed to the Russian radiosonde temperature and humidity sensors with respect the humidity sensors in the European and American radiosondes which are used in the rest of the sites in the present study. Current Russian radiosonde types show relatively slow temperature and humidity sensors, and its measurements of the upper tropospheric humidity also suffers from frequent sensor contamination after passing through cloud (Ingleby, 2017). In addition, in the processing of Russian radiosondes humidity observations, the saturated water vapor pressure still use the same Magnus-like approximation included in the "USSR algorithm" described by Gaffen (1993). A statistics analysis conducted by ECMWF of the mean differences and the root-mean-square differences of the observations from Russian radiosondes and other radiosondes between October 2014 to March 2015, north of 50°N is reported in Fig. 6b in Ingleby et al. (2016). That figure shows the higher values of both statistics in the Russian radiosondes from the surface up to the stratosphere (Ingleby et al., 2016). Further research by the operational ECMWF bias correction system for radiosonde temperature and humidity, for the period January 2015 to December 2016, shows the mean and standard deviation of the bias correction applied (subtracted from reported values) in figure 2.3 in Ingleby (2017). The profiles of the mean and standard deviation of the relative humidity bias correction are higher at all levels for the Russian radiosondes than for the rest of the radiosondes, except for the Chinese and South Korean radiosondes at some levels (Ingleby, 2017).

The results described above make very plausible to attribute the larger values of the STD and MBE for Tiksi in Table 3 and Table S2 to the larger errors of the humidity profiles observations by Russian radiosondes affecting the IWV_{sonde} used in the comparison.

3.5. ΔIWV dependence on $IWV_{sonde,\ j}$ and SZA

Fig. 4 is the scattering plot of $IWV_{sonde,\ j}$ vs. ΔIWV showing a pattern of ΔIWV values distributed around 0. There is a slight increasing tendency of ΔIWV as $IWV_{sonde,\ j}$ increases with a slope 0.05 and intercept 0.032 cm, notorious low values. The Pearson correlation coefficient of 0.378, a very low value, complete the characterization of the weak dependence of ΔIWV with respect to the $IWV_{sonde,\ j}$ magnitudes.

One of the sources of errors on the IWV_{SP} determination is the optical air mass estimation (Kasten and Young, 1989) of several atmospheric components involved in the AERONET water vapor estimation procedure (Giles et al., 2019). Optical air masses depend on solar zenithal angle (SZA). We determined the SZA for $\overline{IWV}_{SP}$ as the maximum from the set of IWV_{SP} used to calculate it for every pair of unconstrained observations in the 30 min time windows. Maximum SZA for the 8 sites is 82.18°, which corresponds with the limit of an optical airmass of 7 given by AERONET version 3 (Giles et al., 2019). In Fig. 5 the scattering plot of SZA vs. ΔIWV is shown. The linear fit shows a negligible decreasing trend with a Pearson correlation coefficient of 0.074, extremely low.

3.6. Relative error estimates

Relative error (RE) from AERONET sun photometer IWV are estimated around 10% in general. Using Eq. (3) we calculated RE for each pair of unconstrained observations in the 30 min time windows and then calculated its frequency distribution. Because of the issues already discussed above regarding the higher sources of errors associated with the IWV_{sonde} at Hornsund and Tiksi they were excluded in the estimation of the RE. Fig. 6 shows the frequency distribution of the RE absolute values. The absolute RE are binned at 1% intervals, showing a regularly decaying pattern from the maximum 12.2% frequency at 2% of RE to 1.1% frequency at 13%. Vertical red discontinuous point out 10% and 15% RE. They illustrate the fact that accumulated RE frequencies up to 10% and 15% RE are 84% and 94% respectively.

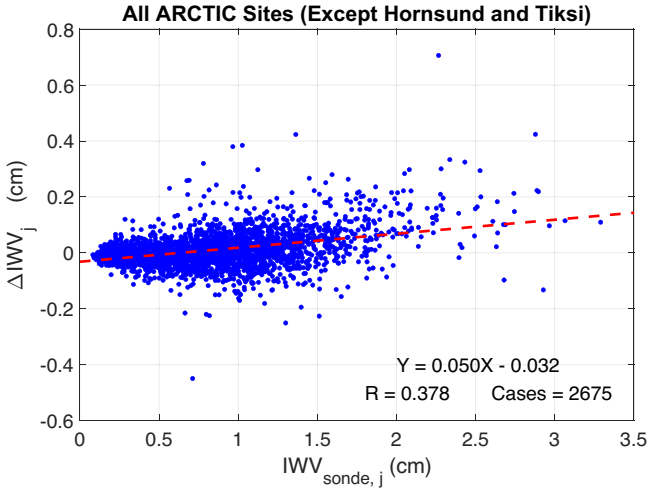

Fig. 4. Scattering plot of ΔIWV_j vs. $IWV_{sonde,\ j}$. The linear fit between both variables is shown by the red discontinuous line. (For interpretation of the references to colour in this figure legend, the reader is referred to the web version of this article.)

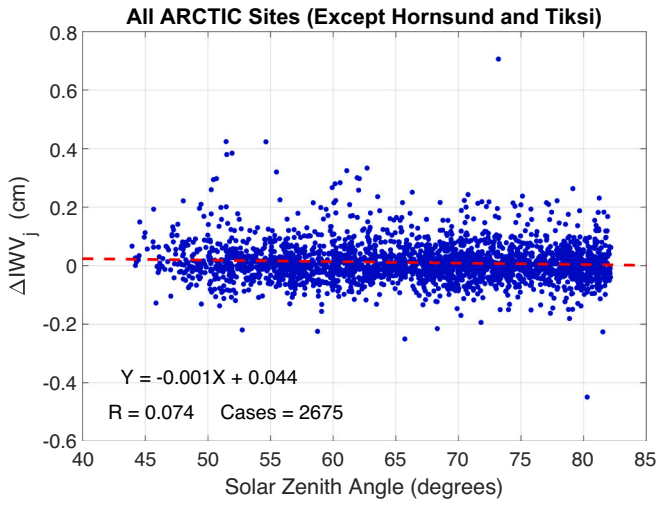

Fig. 5. Scattering plot of ΔIWV_j vs Solar Zenith Angle. The linear fit between both variables is shown by the red discontinuous line. (For interpretation of the references to colour in this figure legend, the reader is referred to the web version of this article.)

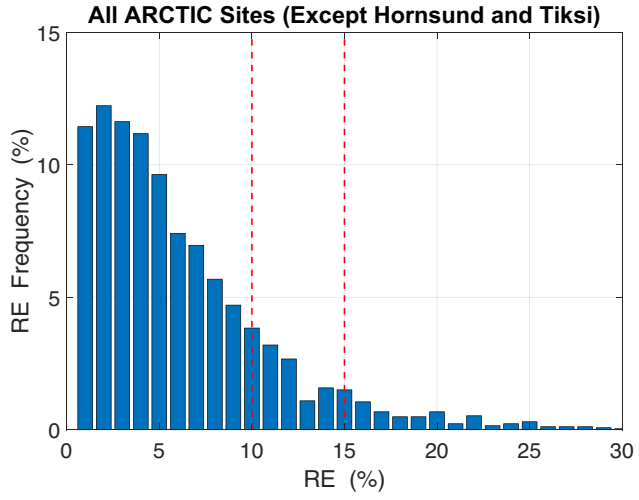

Fig. 6. Frequency distribution of the absolute values of the relative error (RE) magnitudes. RE were binned at 1% intervals. RE accumulated frequencies up to 10% and 15% RE (denoted by the vertical red discontinuous lines placed at 10% and 15% RE) are 84% and 94% respectively. (For interpretation of the references to colour in this figure legend, the reader is referred to the web version of this article.)

4. Conclusions

The most extensive comparison of integrated water vapor (IWV) observations from sun photometers with radiosondes in the Arctic so far has been conducted. The results at Hornsund confirm the importance of using on site radiosonde IWV observations for comparisons. The case of Tiksi confirmed that a careful selection of the radiosonde IWV observations based on the type of humidity sensor will play an important role in the comparison results. The statistics of the comparison between IWV from AERONET sun photometer (IWV_{SP}) and from IGRA-2 radiosondes (IWV_{sonde}), for eight of the Arctic sites (excluding Tiksi and Hornsund sites) in this study are robust. The agreement between IWV_{SP} and IWV_{sonde} observations at the eight selected sites shows a precision of 0.07 cm (7.8%) and an accuracy of 0.01 cm (1.2%) for IWV_{SP} for the 30 min temporal window. The 30 min window seems to be the most suitable choice for the radiosonde-photometer comparison. The comparison of the results among the three temporal windows and the low level of variability in the multiannual hourly means IWV_{SP} at each site demonstrated the relevance of the auto-correlation between intra-diurnal IWV_{SP} observations. This fact could hamper the use of more than one daily mean value of IWV_{SP} for comparisons with IWV observations from other instruments. The differences between the sounding and sun photometer IWV values show a weak dependence on the magnitude of the IWV_{sonde} and a negligible dependence on the solar zenith angle. The general maximum 10% error level of IWV_{SP} observations, when compared with radiosondes, determined until the present mainly for tropical and middle latitudes is also valid in the Arctic. Given the results of the study it is possible to use AERONET observations in the Arctic for water vapor research, considering the robust quantification of its dry bias we have established. Because AERONET uses standard instruments and its centralized-standard processing algorithm, its IWV_{SP} observations are an ideal relative standard dataset to re-calibrate or homogenize the rest of the instrumental IWV observations to a predefined absolute standard dataset like the IWV radiosonde observations.

Author's contribution

J.C. Antuña-Marrero: Writing - Original draft preparation, methodology, algorithm design; R. Roman and V. Cachorro: algorithm and methodology design, discussion, review, project administration and funding acquisition; D. Mateos, methodology design and discussion, A. Calle, C. Toledano, J. C. Antuña-Sánchez and A. de Frutos: methodology design, and discussion; J. Vaquero-Martínez and, M. Antón: discussion and review.

Declaration of Competing Interest

The authors declare that they have no known competing financial interests or personal relationships that could have appeared to influence the work reported in this paper.

Acknowledgements

This research was funded by the Ministerio de Ciencia, Innovación y Universidades (grant no. RTI2018-097864-B-I00) and by Junta de Castilla y León (grant no. VA227P20). Authors also acknowledge funding from Spanish Junta de Extremadura, Consejería de Economía, Ciencia y Agenda Digital, and European Regional Development Fund (ERDF) through Groups Grant (GR21080) and by Junta de Extremadura and ERDF funds through project IB18092. Thanks are due to AERONET-PHOTONS- RIMA staff for providing observations and for the maintenance of the networks. The NOAA National centers for Environmental Information (NCEI) is acknowledged for the provision of the Integrated Global Radiosonde Archive (IGRA) Version 2 radiosonde data used in this publication.

Appendix A. Supplementary data

Supplementary data to this article can be found online at https://doi.org/10.1016/j.atmosres.2022.106059.

References

AERONET, 2021. AERONET Site Lists (V3). https://aeronet.gsfc.nasa.gov/aeronet_locations_v3.txt. Accessed 21/06/2021.

Alexandrov, M.D., Schmid, B., Turner, D.D., Cairns, B., Oinas, V., Lacis, A.A., Gutman, S. I., Westwater, E.R., Smirnov, A., Eilers, J., 2009. Columnar water vapor retrievals from multifilter rotating shadowband radiometer data. J. Geophys. Res. 114, D02306. https://doi.org/10.1029/2008JD010543.

Antón, M., Loyola, D., Román, R., Vömel, H., 2015. Validation of GOME-2/MetOp-A total water vapour column using reference radiosonde data from the GRUAN network. Atmos. Meas. Tech. 8, 1135–1145. https://doi.org/10.5194/amt-8-1135-2015.

Berezin, I.A., Timofeyev, Y.M., Virolainen, Y.A., et al., 2017. Error analysis of integrated water vapor measured by CIMEL photometer. Izv. Atmos. Ocean. Phys. 53, 58–64. https://doi.org/10.1134/S0001433817010030.

Bintanja, R., Selten, F.M., 2014. Future increases in Arctic precipitation linked to local evaporation and sea ice retreat. Nature 509, 479–482.

Box, J.E., Colgan, W., Christensen, T., Schmidt, N., Lund, M., Parmentier, F., Ross Brown, U., Bhatt, E., Euskirchen, V., Romanovsky, J., Walsh, J. Overland, Muyin Wang, R., Corell, W., Meier, B., Wouters, S., Mernild, J., Mård, J., Pawlak, M.S., 2019. Key indicators of Arctic climate change 1971–2017. Environ. Res. Lett. 14, 045010. https://iopscience.iop.org/article/10.1088/1748-9326/aafc1b/meta.

Bright, J.M., Engerer, N.A., Gueymard, C., Killinger, S., Lingfors, D., Sun, X., Wang, P., 2018. Climatic and Global Validation of Daily MODIS Precipitable Water Data at AERONET Sites for Clear-sky Irradiance Modelling. EuroSun 2018 Conf. Proc. 12 https://doi.org/10.18086/eurosun2018.09.07.

Cisek, M., Makuch, P., Petelski, T., 2017. Comparison of meteorological conditions in Svalbard fjords: Hornsund and Kongsfjorden. Oceanologia 59 (4), 413–421. https://doi.org/10.1016/j.oceano.2017.06.004.

Collins, M., Knutti, R., Arblaster, J., Dufresne, J.-L., Fichefet, T., Friedlingstein, P., Gao, X., Gutowski, W.J., Johns, T., Krinner, G., Shongwe, M., Tebaldi, C., Weaver, A. J., Wehner, M.F., Allen, M.R., Andrews, T., Beyerle, U., Bitz, C.M., Bony, S., Booth, B. B.B., 2013. Long-term climate change: Projections, commitments and irreversibility. In: Stocker, T.F., Qin, D., Plattner, G.-K., Tignor, M.M.B., Allen, S.K., Boschung, J., Nauels, A., Xia, Y., Bex, V., Midgley, P.M. (Eds.), Climate Change 2013: The Physical Science Basis. Contribution of Working Group I to the Fifth Assessment Report of the Intergovernmental Panel on Climate Change. Cambridge Univ. Press, pp. 1029–1136. https://www.ipcc.ch/report/ar5/wg1/.

Durre, I., Vose, R.S., Wuertz, D.B., 2006. Overview of the Integrated Global Radiosonde Archive. J. Clim. 19, 53–68. https://doi.org/10.1175/JCLI3594.1.

Durre, I., Williams Jr., C.N., Yin, X., Vose, R.S., 2008. Radiosonde based trends in precipitable water over the Northern Hemisphere: An update. J. Geophys. Res. 114, D05112. https://doi.org/10.1029/2008JD010989.

Durre, I., Vose, R.S., Wuertz, D.B., 2009. Robust automated quality assurance of radiosonde temperatures. J. Appl. Meteorol. Climatol. 47, 2081–2095. https://doi.org/10.1175/2008JAMC1809.1.

Durre, I., Xungang, Y., Vose, Russell S., Applequist, S., Arnfield, J., 2016. Integrated Global Radiosonde Archive (IGRA), Version 2. [PW]. NOAA National Centers for Environmental Information. https://doi.org/10.7289/V5X63K0Q, 22/01/2021.

Durre, I., Yin, X., Vose, R.S., Applequist, S., Arnfield, J., 2018. Enhancing the Data Coverage in the Integrated Global Radiosonde Archive. J. Atmos. Ocean. Technol. 35 (9), 1753–1770. https://doi.org/10.1175/JTECH-D-17-0223.1.

Elgered, G., Johansson, J.M., Rönnäng, B.O., Davis, J.L., 1997. Measuring regional atmospheric water vapor using the Swedish permanent GPS network. Geophys. Res. Lett. 24 (21), 2663–2666. https://doi.org/10.1029/97GL02798.

Forster, P., Ramaswamy, V., Artaxo, P., Berntsen, T., Betts, R., Fahey, D.W., Haywood, J., Lean, J., Lowe, D.C., Myhre, G., Nganga, J., Prinn, R., Raga, G., Schulz, M., Van Dorland, R., 2007. Changes in atmospheric constituents and in radiative forcing. In: Solomon, S., Qin, D., Manning, M., Chen, Z., Marquis, M., Averyt, K.B., Tignor, M., Miller, H.L. (Eds.), Climate Change, The Physical Science Basis. Contribution of Working Group I to the Fourth Assessment Report of the Intergovernmental Panel on Climate Change. Cambridge University Press, Cambridge, United Kingdom and New York, NY, USA. https://www.ipcc.ch/report/ar4/wg1/.

Gaffen, D.J., 1993. Historical changes in radiosonde instruments and practices: final report. 123 pp. WMO/TD-No. 541; IOM Report-No. 50. http://library.wmo.int/pmb_ged/wmotd_541_en.pdf.

Giles, D.M., Sinyuk, A., Sorokin, M.G., Schafer, J.S., Smirnov, A., Slutsker, I., Eck, T.F., Holben, B.N., Lewis, J.R., Campbell, J.R., Welton, E.J., Korkin, S.V., Lyapustin, A.I., 2019. Advancements in the Aerosol Robotic Network (AERONET) Version 3 database – automated near-real-time quality control algorithm with improved cloud screening for Sun photometer aerosol optical depth (AOD) measurements. Atmos. Meas. Tech. 12, 169–209. https://doi.org/10.5194/amt-12-169-2019.

Gong, S., Chen, W., Zhang, C., Wu, P., Han, J., 2020. Intercomparisons of precipitable water vapour derived from radiosonde, GPS and sunphotometer observations. Geodetski Vestnik 64, 562–577. https://doi.org/10.15292/geodetski-vestnik.2020.04.562-577.

Ingleby, B., 2017. An assessment of different radiosonde types 2015/2016. ECMWF Technical Memoranda, European Centre for Medium-Range Weather Forecasts. https://doi.org/10.21957/0nje0wpsa.

Ingleby, B., Rodwell, M., Isaksen, L., 2016. Global radiosonde network under pressure. ECMWF newsletter 149, 25–30. http://www.ecmwf.int/en/about/media-centre/media-resources.

Kasten, F., Young, A.T., 1989. Revised optical air mass tables and approximation formula. Appl. Opt. 28, 4735–4738. https://doi.org/10.1364/AO.28.004735.

Kruczyk, M., Liwosz, T., 2015. Integrated Precipitable Water Vapour Measurements at Polish Polar Site Hornsund from GPS Observations Verified by Aerological Techniques. Reports on Geodesy and Geoinformatics 98, 1–17. https://doi.org/10.2478/rgg-2015-0001.

Leblanc, T., Walsh, T.D., McDermid, I.S., Toon, G.C., Blavier, J.-F., Haines, B., Read, W. G., Herman, B., Fetzer, E., Sander, S., Pongetti, T., Whiteman, D.N., McGee, T.G., Twigg, L., Sumnicht, G., Venable, D., Calhoun, M., Dirisu, A., Hurst, D., Jordan, A., Hall, E., Miloshevich, L., Vömel, H., Straub, C., Kampfer, N., Nedoluha, G.E., Gomez, R.M., Holub, K., Gutman, S., Braun, J., Vanhove, T., Stiller, G., Hauchecorne, A., 2011. Measurements of Humidity in the Atmosphere and Validation experiments (MOHAVE)-2009: overview of campaign operations and results. Atmos. Meas. Tech. 4, 2579–2605. https://doi.org/10.5194/amt-4-2579-2011.

Pérez-Ramírez, D., Navas-Guzmán, F., Lyamani, H., Fernández-Gálvez, J., Olmo, F.J., Alados-Arboledas, L., 2012. Retrievals of precipitable water vapor using star photometry: Assessment with Raman lidar and link to sun photometry. J. Geophys. Res. Atmos. 117, D05202.

Pérez-Ramírez, D., Whiteman, D.N., Smirnov, A., Lyamani, H., Holben, B.N., Pinker, R., Andrade, M., Alados-Arboledas, L., 2014. Evaluation of AERONET precipitable water vapor versus microwave radiometry, GPS, and radiosondes at ARM sites. J. Geophys. Res. Atmos. 119, 9596–9613. https://doi.org/10.1002/2014JD021730.

Przybylak, R., Araźny, A., 2006. Climatic conditions of the northwestern part of Oscar II Land (Spitsbergen) in the period between 975 and 2000. Pol. Polar Res. 27 (2), 133–152. https://repozytorium.umk.pl/handle/item/3069.

Román, R., Antón, M., Cachorro, V.E., Loyola, D., Ortiz de Galisteo, J.P., de Frutos, A., Romero-Campos, P.M., 2015. Comparison of total water vapor column from GOME-2 on MetOp-A against ground-based GPS measurements at the Iberian Peninsula. Sci. Total Environ. 533, 317–328. https://doi.org/10.1016/j.scitotenv.2015.06.124.

Schmid, B., Michalsky, J.J., Slater, D.W., Barnard, J.C., Halthore, R.N., Liljegren, J.C., Holben, B.N., Eck, T.F., Livingston, J.M., Russell, P.B., Ingold, T., Slutsker, I., 2001. Comparison of columnar water-vapor measurements from solar transmittance methods. Appl. Opt. 40, 1886–1896.

Schneider, M., Romero, P.M., Hase, F., Blumenstock, T., Cuevas, E., Ramos, R., 2010. Continuous quality assessment of atmospheric water vapour measurement techniques: FTIR, Cimel, MFRSR, GPS, and Vaisala RS92. Atmos. Meas. Tech. 3, 323–338. https://doi.org/10.5194/amt-3-323-2010.

Schröder, M., Lockhoff, M., Shi, L., August, T., Bennartz, R., Borbas, E., Brogniez, H., Calbet, X., Crewell, S., Eikenberg, S., Fell,F., Forsythe, J., Gambacorta, A., Graw, K., Ho, S.-P., Höschen, H., Kinzel, J., Kursinski, E. R., Reale, A., Roman, J., Scott, N., Steinke, S., Sun, B., Trent, T.,Walther, A.,Willen, U., and Yang, Q., 2017, GEWEX water vapor assessment (G-VAP), WCRP Report16/2017, World Climate Research Programme (WCRP): Geneva, Switzerland, 216 pp. https://www.wcrp-climate.org/resources/wcrp-publications.

Steinke, S., Eikenberg, S., Löhnert, U., Dick, G., Klocke, D., Di Girolamo, P., Crewell, S., 2015. Assessment of small-scale integrated water vapour variability during HOPE. Atmos. Chem. Phys. 15, 2675–2692. https://doi.org/10.5194/acp-15-2675-2015.

Van Malderen, R., Brenot, H., Pottiaux, E., Beirle, S., Hermans, C., De Mazière, M., Wagner, T., De Backer, H., Bruyninx, C., 2014. A multi-site intercomparison of integrated water vapour observations for climate change analysis. Atmos. Meas. Tech. 7, 2487–2512. https://doi.org/10.5194/amt-7-2487-2014.

Vaquero-Martinez, J., Anton, M., 2021. Review on the Role of GNSS Meteorology in monitoring Water Vapor for Atmospheric Physics. Remote Sens. 13, 2287. https://doi.org/10.3390/rS23122287.

Vaquero-Martínez, J., Antón, M., Ortiz de Galisteo, J.P., Cachorro, V.E., Álvarez-Zapatero, P., Román, R., Loyola, D., Costa, M.J., Wang, H., Gonzalez-Abad, G., Noel, S., 2018. Inter-comparison of integrated water vapor from satellite instruments using reference GPS data at the Iberian Peninsula. Remote Sens. Environ. 204, 729–740. https://doi.org/10.1016/j.rse.2017.09.028.

Vaquero-Martínez, J., Antón, M., Ortiz de Galisteo, J.P., Román, R., Cachorro, V.E., Mateos, D., 2019. Comparison of integrated water vapor from GNSS and radiosounding at four GRUAN stations. Sci. Total Environ. 648, 1639–1648. https://doi.org/10.1016/j.scitotenv.2018.08.192.

Vaquero-Martínez, J., Antón, M., Román, R., Cachorro, V.E., Wang, H., González-Abad, G., Ritter, C., 2020. Water vapor satellite products in the European Arctic: an inter-comparison against GNSS data. Sci. Total Environ. 741, 140335 https://doi.org/10.1016/j.scitotenv.2020.140335.

Vihma, T., Screen, J., Tjernström, M., Newton, B., Zhang, X., Popova, V., Deser, C., Holland, M., Prowse, T., 2016. The atmospheric role in the Arctic water cycle: a review on processes, past and future changes, and their impacts. J. Geophys. Res. Biogeosci. 121, 586–620. https://doi.org/10.1002/2015JG003132.

Vogelmann, H., Sussmann, R., Trickl, T., Reichert, A., 2015. Spatiotemporal variability of water vapor investigated using lidar and FTIR vertical soundings above the Zugspitze. Atmos. Chem. Phys. 15, 3135–3148. https://doi.org/10.5194/acp-15-3135-2015.

Wang, R., Liu, Y., 2020. Recent declines in global water vapor from MODIS products: Artifact or real trend? Remote Sens. Environ. 247, 111896 https://doi.org/10.1016/j.rse.2020.111896.

Weaver, D., Strong, K., Schneider, M., Rowe, P.M., Sioris, C., Walker, K.A., Mariani, Z., Uttal, T., McElroy, C.T., Vömel, H., Spassiani, A., Drummond, J.R., 2017. Intercomparison of atmospheric water vapour measurements at a Canadian High Arctic site. Atmos. Meas. Tech. 10, 2851–2880. https://doi.org/10.5194/amt-10-2851-2017.

Whiteman, D.N., Cadirola, M., Venable, D., Calhoun, M., Miloshevich, L., Vermeesch, K., Twigg, L., Dirisu, A., Hurst, D., Hall, E., Jordan, A., Vömel, H., 2012. Correction technique for Raman water vapor lidar signal-dependent bias and suitability for water vapor trend monitoring in the upper troposphere. Atmos. Meas. Tech. 5, 2893–2916. https://doi.org/10.5194/amt-5-2893-2012.